RESEARCH ARTICLE

**Magnetic Resonance in Medicine**

# Development of an echo-shifted, multi-echo, gradient-echo sequence for T$_2$* quantification of slow-relaxing water pools

**Seonyeong Shin**[1,2] | **Ana-Maria Oros-Peusquens**[1] | **Seong Dae Yun**[1] | **Ezequiel Farrher**[1] | **N. Jon Shah**[1,3,4,5]

[1]Institute of Neuroscience and Medicine 4, INM-4, Forschungszentrum Jülich, Jülich, Germany

[2]RWTH Aachen University, Aachen, Germany

[3]Institute of Neuroscience and Medicine 11, INM-11, JARA, Forschungszentrum Jülich, Jülich, Germany

[4]JARA - BRAIN - Translational Medicine, Aachen, Germany

[5]Department of Neurology, RWTH Aachen University, Aachen, Germany

**Correspondence**
N. Jon Shah, Institute of Neuroscience and Medicine 4, INM-4, Forschungszentrum Jülich, 52428 Jülich, Germany.
Email: n.j.shah@fz-juelich.de

## Abstract

**Purpose:** Although conventional multi-echo gradient-echo (GRE) sequences effectively quantify short and intermediate T$_2$* in brain tissue, and general interest in cerebrospinal fluid (CSF) is growing due to its association with the glymphatic system, quantifying T$_2$* in CSF remains underexplored. Accurate quantification of the slow-relaxing water pools requires imaging at long echo times, significantly increasing acquisition time. This study proposes a novel sequence capable of quantifying the entire range of T$_2$* without prolonged acquisition time, mapping T$_2$* in both CSF and brain tissue.

**Methods:** The proposed echo-shifted, multi-echo GRE (ES-mGRE) combines the conventional multi-echo GRE sequence with an echo-shifting technique. Additional gradients are introduced, producing echoes in the next sub–repetition time interval.

**Results:** ES-mGRE generates artifact-free images at both short and long echo times without extending acquisition time. Increasing the area of the additional gradients enhances diffusion sensitivity, allowing simultaneous quantification of T$_2$* and $D$ in CSF. The mean T$_2$* of white matter and gray matter is 55.9 ms and 51.5 ms at 3 T, respectively. The mean T$_2$* in the ventricles is 234.5 ms. The simultaneously quantified mean $D$ value of 3.07 μm$^2$/ms is closely aligned with the reference diffusivity.

**Conclusion:** We demonstrate that the proposed ES-mGRE sequence can effectively quantify the T$_2$* of both CSF and brain tissue while also providing simultaneous diffusion information.

**KEYWORDS**
diffusivity, echo-shifting technique, multi-echo gradient echo, quantitative parameter mapping, T$_2$* relaxation time

---

Seonyeong Shin and Ana-Maria Oros-Peusquens contributed equally to this work.

# 1 | INTRODUCTION

Cerebrospinal fluid (CSF) is clinically significant in the diagnosis of various diseases and is routinely analyzed to detect biomarkers for brain conditions such as infections or inflammations of the central nervous system. Recently, CSF has also been used for liquid biopsies in glioma diagnosis.[1] Lumbar puncture remains the typical method used for this procedure.

Interest in CSF has grown due to its role in the glymphatic system, which is hypothesized to function as a brain waste clearance system.[2–4] Quantitative MRI (qMRI) enables the noninvasive quantification of tissue properties such as $T_1$, $T_2$, $T_2^*$, diffusion, or flow, which may serve as biomarkers for brain disease and have been the focus of recent studies.[5–8]

The $T_2^*$ relaxation time can be measured, for example, using the quantitative $T_2^*$ image (QUTE) sequence,[9–11] a variant of the multi-echo gradient-echo (mGRE) sequence. QUTE obtains multiple echoes via a bipolar readout and uses a multislice acquisition method, facilitating accurate $T_2^*$ mapping with whole-brain coverage. The in-house-developed mGRE sequence was originally reported in Shah et al.[9] and Dierkes et al.[10] under the acronym QUTE (quantitative $T_2^*$ image). We have continued to use this acronym in several related publications[11–15]; however, because the sequence is a multi-echo gradient echo implementation with bipolar readout, herein we will use, in most instances, the terms "in-house-implemented mGRE" and "echo-shifted mGRE" instead of the acronyms QUTE and ES-QUTE, which were used when reporting our preliminary results.[16,17]

Although mGRE sequences efficiently measure $T_2^*$ in brain parenchyma, research relating to $T_2^*$ in CSF remains limited. If $T_2^*$ in CSF can be shown to correlate with glymphatic clearance, it could be further explored in relation to neurodegenerative diseases.

While the number of echoes used for $T_2^*$ mapping is important for the fit performance, the time interval spanned by these echoes needs to extend to at least $T_2^*$ for each tissue type for optimal performance.[11] Gray and white matter have relatively comparable $T_2^*$ at 3 T[9–11]; however, $T_2^*$ values in CSF are an order of magnitude longer compared with brain tissue, requiring a much longer interval of TE values for similar performance of quantification. A long maximum TE is generally accompanied by an increase in TR, which in turn prolongs the acquisition time. Although the acquisition time can be reduced by using, for example, parallel-imaging techniques, acceleration is constrained by the coil configuration and required signal-to-noise ratio (SNR).[18,19] The main drawback of attempting to quantify the $T_2^*$ of both brain parenchyma and CSF with comparable accuracy is that a large fraction of the measurement time is spent acquiring echoes that do not contribute to the characterization of the already decayed brain-tissue signal (Figure 1C).

Moonen et al.[20] first proposed an echo-shifting technique in which spins excited by a radiofrequency (RF) pulse are refocused in the subsequent repetition-time (TR) interval via additional gradients, enabling the acquisition of long echo-time (TE) images within a minimal scan time. However, RF pulses in subsequent TR intervals might interfere with the signal of interest.[21] To mitigate this, echo-shifting techniques are often paired with multislice acquisition methods.[22,23]

In this work, the echo-shifting technique was extended to the mGRE sequence for $T_2^*$ quantification of both CSF and brain tissue. The proposed sequence, echo-shifted multi-echo GRE (ES-mGRE) makes use of multislice acquisition to acquire both short-TE and long-TE images without extending scan time. In this work, ES-mGRE was validated at 3 T using phantom and in vivo experiments, and the results demonstrate close alignment with the reference methods.

# 2 | THEORY

Figure 1A shows a schematic diagram of the proposed sequence. ES-mGRE combines an mGRE sequence[9–11] with an echo-shifting technique. In the following, a detailed description of the gradient characteristics is provided.

1. Readout and additional gradients: To acquire multiple echo data, a gradient reversal process is repeated as in conventional mGRE. A number of echoes, $p$, are first obtained. Both polarities of the readout gradients are used to obtain a larger number of echoes with a shorter echo-spacing time than would be the case with a typical monopolar readout. Following the acquisition of $p$ echoes, spins excited by $n$th RF pulse are then dephased with the first *additional* gradient $(-A')$. The dephased spins are rephased after the second gradient $(+2A')$ and the first additional gradient *in the next sub-TR interval*. A number of echoes, $q$, are subsequently collected at long TEs. Spins excited by the $(n + 1)$th RF pulse in the next slice do not contribute to the echo-shifted signals, as they are already dephased by the first additional gradient. This procedure is iterated. As a result, the readout period is separated into two parts: Section 1 collects the normal echoes, and Section 2 acquires the shifted echoes from the previous slice. The aim of this is to quantify short, intermediate,
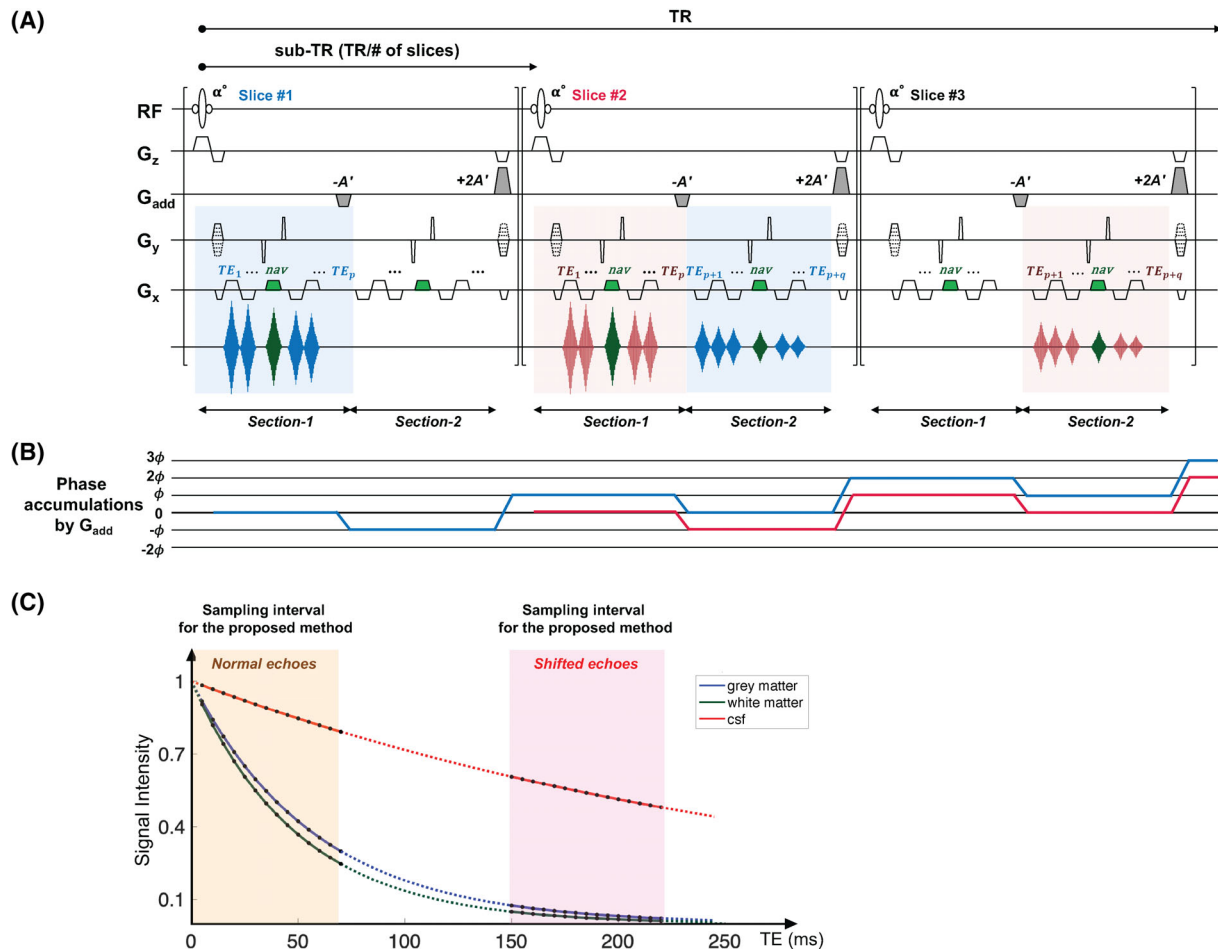
**FIGURE 1** (A) Schematic diagram of the proposed echo-shifted, multi-echo gradient echo. (B) Corresponding phase plot. (C) Signal decay of gray matter, white matter, and cerebrospinal fluid (CSF). The colored areas indicate the time intervals during which the signals are sampled by the proposed method. The interval in between, where the expected signal decay is indicated with a dotted line, is not sampled. RF, radiofrequency; TE, echo time; TR, repetition time.

and long $T_2^*$ by sampling the front and rear parts of the signal decay. After collecting $(p + q)$ echoes, the read-out dephasing gradient is duplicated at the end of each sub-TR interval. If the total number of echoes, $(p + q)$, is an even number, gradients with the same strengths but opposite polarities are employed.

The additional echo-shifting gradients can, theoretically, be introduced along any axis. In addition, these gradients serve as diffusion-weighting gradients, potentially enabling the measurement of diffusion properties.

2. Phase-encoding gradients: A phase-encoding gradient is applied at the beginning of each TR, and the gradient strength is incremented to cover the k-space. Motion due to physiological processes, such as respiration or pulsation, is known to induce field variations in tissue, which can result in image artifacts and distort parameter quantification.[24,25] To minimize

the effects of such field fluctuations, the acquisition of navigator echoes is incorporated and used for postprocessing corrections (see area in green). A phase rewinding and a winding gradient are applied before and after the navigator echo, respectively, within the shortest possible time. Following the acquisition of $(p + q)$ echoes, the phase-encoding gradient is rewound.

3. Slice-selection gradients: A slice-selection and a slice-refocusing gradient are used at the beginning of each TR. The refocusing gradient is duplicated following the acquisition period.

Figure 1B shows the plots of phase accumulation induced by the additional gradients. The net phase becomes zero at the location of the echo read out. After the acquisition of shifted echoes, the spins excited by $n$th RF pulse are gradually spoiled by additional gradients in the subsequent sub-TR intervals.

## 3 | METHODS

### 3.1 | Computer simulations

Computer simulations were performed to investigate the effect of echo-shifting on $T_2^*$ quantification and to optimize imaging parameters. A detailed explanation of the computer simulations and parameter setting are provided in the Supporting Information. Because ES-mGRE uses a multislice acquisition method with a single RF pulse per slice and effective TR (TR for both prompt and shifted echoes), the signal equation is equivalent to that of a spoiled GRE. This is in contrast to the signal loss that occurs in echo shifting with a single slice excitation, which involves multiple RF pulses per effective TR.[23] Thus, the signal decay over time was adapted from that of spoiled GRE:

$$s(\text{TE}_n) = M_0 \left( \frac{\sin(\alpha)\left(1 - e^{-\text{TR}/T_1}\right)}{1 - \cos(\alpha)e^{-\text{TR}/T_1}} \right) e^{-\text{TE}_n/T_2^*} e^{1i(\phi_0 + 2\pi\Delta f \text{TE}_n)}$$
$$\times e^{-b(\text{TE}_n)D} + \varepsilon\left(0, \sigma^2\right), \quad (1)$$

where $s(\text{TE}_n)$ represents the signal obtained at the $n$th TE; $M_0$ is the spin density; and $\alpha$ is the flip angle. $T_1$ and $T_2^*$ are the longitudinal and effective transverse relaxation times, respectively; $\phi_0$ is an initial phase; $\Delta f$ is the off-resonance frequency; $b(\text{TE}_n)$ is the diffusion-weighting $b$-value induced by additional gradients; and $D$ represents the diffusion coefficient of each compartment. $\varepsilon(0, \sigma^2)$ refers to additive white Gaussian noise.

Data sets consisting of 24, 32, and 64 echoes were created, each with $K$ values of 4, 8, 10, 12, and 16. The value of $K$ describes the area of the first additional gradient, set to $K$ times that of the slice rephasing gradient. To determine how many echoes need to be shifted to provide reliable results, the number of shifted echoes was varied from 0 to $N$, the number of total echoes. The produced data sets were fitted as described in Section 3.5.

### 3.2 | Phantom experiments

Phantom experiments were performed on a 3T MR scanner (MAGNETOM Prisma; Siemens Healthineers, Erlangen, Germany). A total of 12 data sets (i.e., 24, 32 and 64 echoes × $K$ of 4, 8, 10, and 12) were obtained with the following imaging parameters: field of view (FOV) = 240 × 216 mm², matrix size = 240 × 216, slice thickness = 2 mm, TR = 1200 ms, flip angle = 75°, pixel bandwidth = 800 Hz/px, $\text{TE}_1$ = 3 ms, $\Delta$TE = 1.47 ms, $\Delta$PE = 0.8 ms (the time required for phase rewinding and winding gradients), and direction of additional gradients = slice selection. One-third of the echoes were shifted to the next sub-TR interval. Two navigator echoes were acquired in the middle of the normal and shifted echo train, respectively. The number of slices, $b$-values, and TEs of the shifted echoes for each data set are described in Table S1.

Reference acquisitions of $T_2^*$ and $D$ values were performed using in-house-implemented mGRE, QUTE,[9–11] and the manufacturer's spin-echo, diffusion-weighted, echo-planar imaging (DW-EPI), respectively. The QUTE data sets were acquired with the same imaging parameters as the ES-mGRE, but with double the TR and number of echoes: TR = 2400 ms, number of echoes = 157 (including four navigator echoes located at Echoes 20, 59, 98, and 137). The DW-EPI data sets were obtained with FOV = 240 × 216 mm², matrix size = 240 × 216, slice thickness = 2 mm, TR = 5000 ms, number of slices = 24, pixel bandwidth = 1096 Hz/px, TE = 90 ms, GRAPPA acceleration factor = 2, partial Fourier factor = 6/8, and $b$-value = 0, 20, 30, 40, 60, 80, 100, 200, 400, 600, 800, and 1000 s/mm². The reference $D$ values were also restricted to the slice-selection direction, $D_z$, with all the $b$-values considered for the calculation.

### 3.3 | In vivo experiments

In vivo data sets were obtained from 4 healthy volunteers. All subjects provided written, informed consent before the study. Imaging parameters were configured as in the first column of Table 1. The in-plane resolution was kept at 1 × 1 mm². The phase FOV (left–right direction) was adjusted for the head of each subject to minimize the scan time. Forty-three of 64 echoes were prompt, and 21 shifted to the next sub-TR interval, thereby ensuring sufficient sampling of the signal decay from both brain tissue and CSF. The TEs of the shifted echoes ranged from 206.88 to 237.72 ms, and the $b$-values were about 180 s/mm², corresponding to a value of $K$ = 10, optimized according to computer simulation and phantom experiments.

For comparison, data sets were also obtained using in-house-implemented mGRE, QUTE.[9–11] Imaging parameters that primarily affect SNR (e.g., TR, flip angle, bandwidth) were the same as those for ES-mGRE but with an increased number of echoes to cover a similar TE range (second column). The vendor-implemented Siemens mGRE sequence, which only allows for the acquisition of 12 echoes, was configured to have the same TE range as the unshifted echoes in ES-mGRE, in-plane resolution = 1.1 × 1.1 mm², $\text{TE}_1$ = 3 ms, $\Delta$TE = 5.8 ms. The reference diffusivity values were acquired using DW-EPI. A three-dimensional (3D) magnetization-prepared rapid gradient-echo sequence was included for brain tissue segmentation (Table S2).

**TABLE 1**   Imaging parameters for in vivo experiments.

| | ES-mGRE | In-house-implemented mGRE, QUTE |
|---|---|---|
| TR | 3000 ms | |
| Flip angle | 60° | |
| FOV read | 240 mm | |
| In-plane resolution | $1 \times 1$ mm$^2$ | |
| Slice thickness | 2 mm | |
| Bandwidth | 800 Hz/px | |
| # of slices | 23 | 11 |
| # of echoes | 64 | 157 |
| # of navigators | 2 | 4 |
| (location) | (16th, 49th) | (20th, 59th, 98th, 137th) |
| # of shifted echoes | 21 | - |
| $K$ ($b$-value of the shifted echoes) | 10 ($\approx 250$ s/mm$^2$) | - |
| TEs | TE$_1$ = 3 ms TE$_{43}$ = 66.18 ms TE$_{44}$ = 206.88 ms TE$_{64}$ = 237.72 ms | TE$_1$ = 3 ms TE$_{157}$ = 238.08 ms |
| ΔTE | 1.47 ms | |
| ΔPE | 0.8 ms | |

Abbreviations: ES, mGRE, echo-shifted multi-echo gradient echo; FOV, field of view; PE, phase encoding; QUTE, quantitative T$_2$* image; TE, echo time; TR, repetition time.

## 3.4 | Postprocessing

Navigator echo correction was performed to compensate for field variations caused by physiological motion or, possibly, system drift from scanner instability. The correction method outlined in Refs. [24,25] was modified for our study. Due to the very long TE interval and echo train used in our experiments, we found it necessary to acquire more than one navigator echo. This allows one to correct for variations occurring between phase-encoding steps and during the echo train.

Two navigator echoes were acquired for ES-mGRE: one in the middle of the unshifted echoes ($N_u$) and the other in the middle of the shifted echoes ($N_s$). The correction of ES-mGRE data sets consists of two steps. First, a one-dimensional (1D) Fourier transform was applied to all readouts. In the first step, the phase differences between the first and $p$th phase-encoding steps were calculated using the phase of the first navigator echo. The 1D Fourier-transformed k-space lines of each echo, shifted and unshifted, as well as of later navigator echoes, were then corrected by multiplying the phase differences with the TEs, as follows:

$$s_p^c\left(x, k_y, \text{TE}_n\right) = s_p\left(x, k_y, \text{TE}_n\right) e^{-i \frac{\phi_{Nup}\left(x,k_y\right) - \phi_{Nu1}\left(x,k_y\right)}{\text{TE}_{nav1}} \cdot \text{TE}_n}, \quad (2a)$$

where $s_p^c(x, k_y, \text{TE}_n)$ and $s_p(x, k_y, \text{TE}_n)$ are the 1D Fourier-transformed k-space signals after and before the

correction, respectively; TE$_{nav1}$ is the TE of the first navigator echo; and $\phi_{Nup}(x,k_y) - \phi_{Nu1}(x,k_y)$ represents the phase difference calculated between the first navigator of k-space line $p$ and the first navigator of k-space line 1. In the second step, we calculate the phase differences involving the second navigator echoes, which have already been corrected by the first navigator as in Eq. (2a). The differences were then used to correct only the shifted echoes as follows:

$$s_p^c\left(x, k_y, \text{TE}_n\right) = s_p\left(x, k_y, \text{TE}_n\right) e^{-i \frac{\phi_{N_{sp}}^c\left(x,k_y\right) - \phi_{N_{s1}}^c\left(x,k_y\right)}{\text{TE}_{nav2}} \cdot \text{TE}_n},$$
only for shifted echoes. (2b)

For the in-house-implemented mGRE-QUTE acquisition, which uses more echoes to cover the same TE interval, four navigators were acquired. Each navigator was used to phase-correct the closet echoes in the second step. For example, in a 128-echo acquisition with four navigators, Echoes 1–32 were corrected by the first navigator only, Echoes 33–64 by the first and second navigators (Eqs. [2a] and [2b]), Echoes 65–96 by the first and third navigators, and Echoes 97–128 by the first and fourth navigators.

## 3.5 | Fitting and analysis

The corrected k-space data of individual coils were Fourier-transformed and combined using an adaptive combine method.[26] As stated in Section 2, using additional

gradients adds a diffusion-weighting effect to the images. Thus, $T_2^*$ quantification was performed and compared without and with consideration of the diffusion effects.

$$s(TE_n) = M_0 e^{-TE_n/T_2^*} e^{-b(TE_n) \cdot D} e^{(-1)^n \delta}. \quad (3)$$

Equation (3) is an adaptation of Eq. (1) relevant to $T_2^*$ fitting. Here, the diffusion weighting (*b*-factor) and the bipolar readout (δ modulation) are directly included, whereas steady-state effects ($T_1$, flip angle) are included in the signal intensity at $TE = 0$ ms. The *b*-values were computed from all imaging gradients except for the phase-encoding gradients.[27] As the data sets were acquired using bipolar readouts, amplitude modulation δ was considered[28] and corrected with an iterative fitting, similar to that described in Refs. [29] and [30] by finding the value that minimizes the differences between acquired and synthesized images generated without δ. In computer simulations, δ was excluded, as the data sets were generated under conditions ideal for focusing only on the echo-shifting gradient effects. For in-house-implemented mGRE, QUTE, and for the vendor-implemented Siemens mGRE data sets, the diffusion term was neglected.

When the signal predominantly contains noise, which is often the case for long TEs, the fit of the magnitude signal can lead to an overestimation of $T_2^*$.[31,32] To avoid this bias, Rician noise distribution was incorporated in the fitting process.[33] The noise variance was determined based on four ROIs positioned at the corners of the background, each consisting of 400 voxels.

To assess the accuracy and precision, the mean and standard deviation of the calculated $T_2^*$ and $D$ were measured. In the case of in vivo experiments, segmentation results obtained using *FreeSurfer* were used as masks.[34,35]

## 4 | RESULTS

Figure 2 shows the results of computer simulations. Figure 2A displays the images for the different TE values, with the third and fourth rows corresponding to the shifted echo images. The quantified parameter maps are presented alongside the reference maps. The signal decay of brain tissue can be sufficiently sampled during the acquisition of the unshifted echoes. Because of its long TE values, only the signal from CSF remains in the shifted echo images. Incorporating the effect of diffusion into the signal model produces $T_2^*$ values that are closer to the ground-truth values. For the brain tissue with relatively low diffusivity, the quantified $T_2^*$ values remained consistent, regardless of whether the diffusion was included in the model. Figure 2B displays plots of the signal decay and *b*-values versus TE in the simulated CSF region when the number of echoes was set to 64. Each color represents a different area of the additional gradients, and thus a different diffusion weighting. As the area of additional gradients ($K$) increases, the signal intensity of the shifted echoes decreases and the shifted TEs increase,
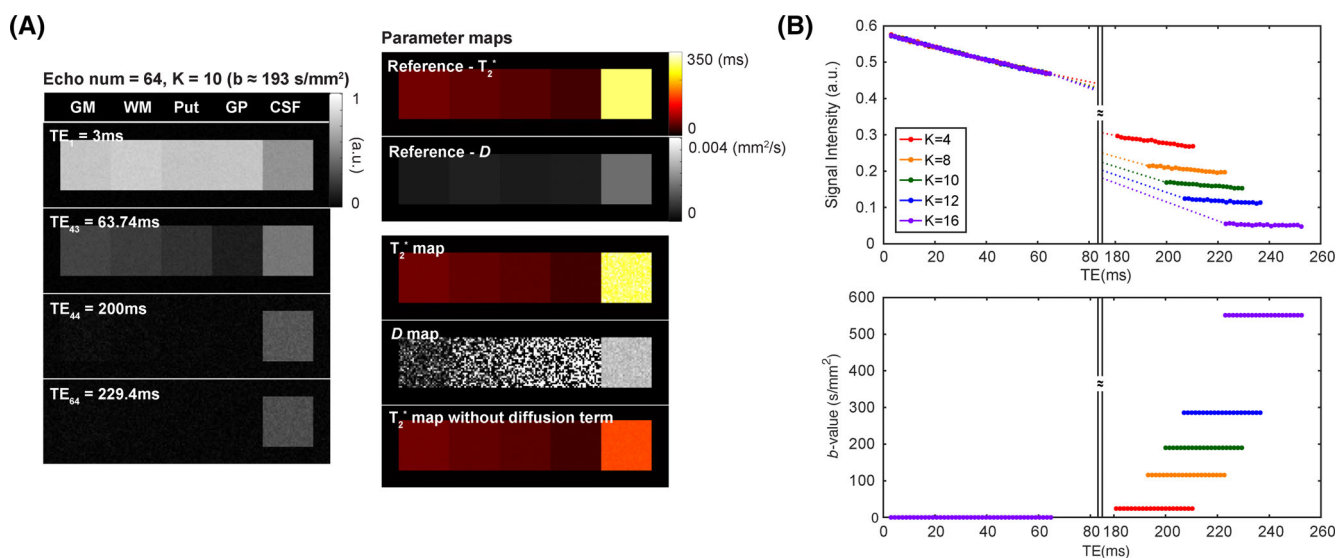


**FIGURE 2** (A) Simulation data sets generated with 64 echoes and $K$ equal to 10. One-third of the total echoes were shifted. Each small rectangular region illustrates the expected behavior of different brain regions: gray matter (GM), white matter (WM), putamen (Put), globus pallidus (GP), and cerebrospinal fluid (CSF). (B) Plots of the signal decay versus echo time (TE) and *b*-value versus TE in the cerebrospinal fluid (CSF) region for 64 echoes and various values of $K$. The parameter $K$ scales the integral of the echo-shifting gradients, thereby modulating diffusion sensitivity and signal reduction of the shifted echoes.
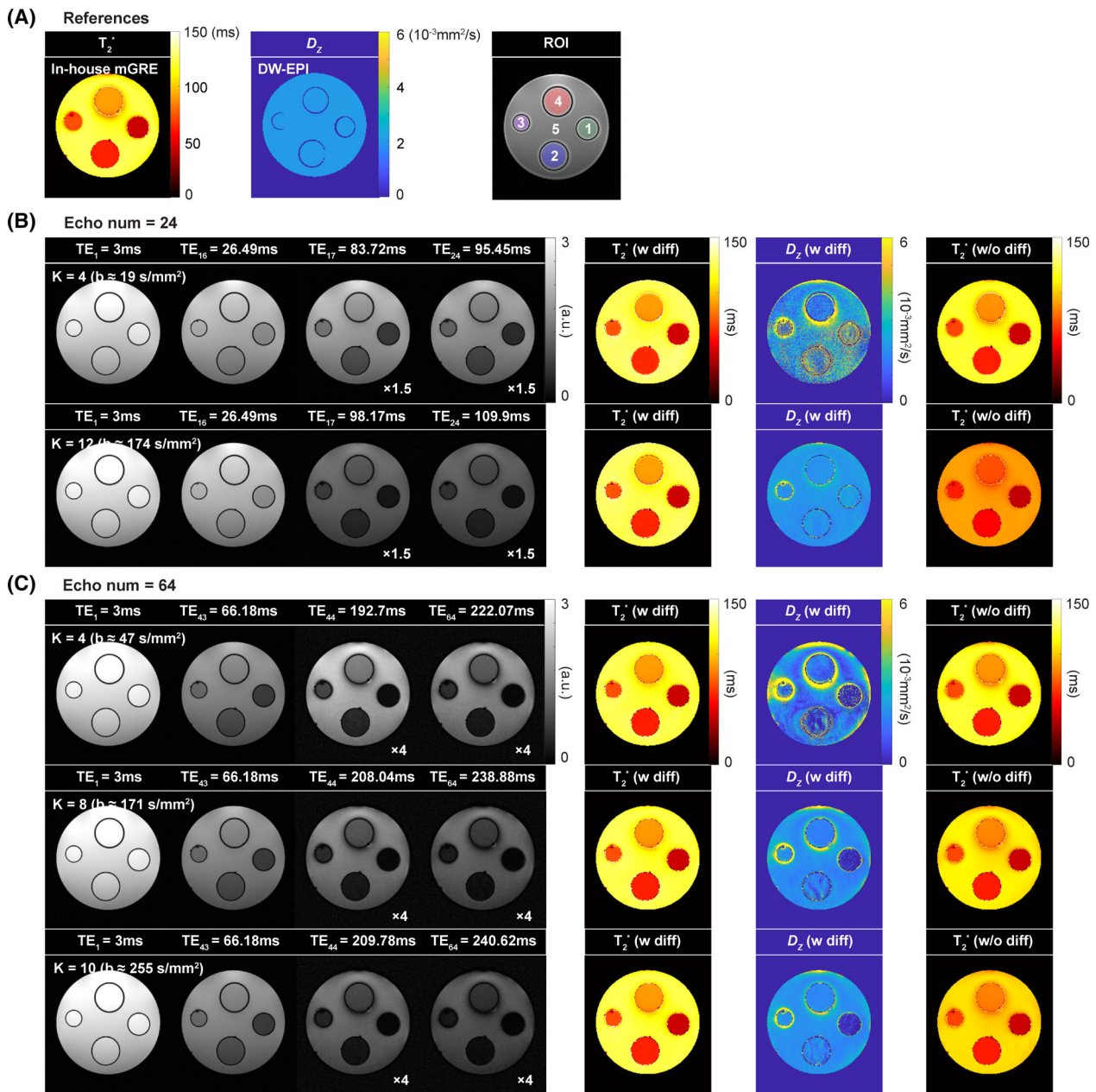
**FIGURE 3** Results of phantom experiments obtained from reference (A) and data sets having 24 (B) and 64 (C) echoes. In (B) and (C), the first two columns show the normal (i.e., unshifted) echo images, whereas the third and fourth columns show the shifted echo images. The fifth to seventh columns depict the calculated quantitative maps with and without considering the diffusion term, respectively. Each row represents the results for different areas of additional gradients. The results with the different number of echoes and $K$ can be found in Figure S3. DW-EPI, diffusion-weighted echo-planar imaging; ROI, region of interest; TE, echo time.

as described in the Computer Simulations section in the Supporting Information. More detailed simulation results demonstrating the effects of the number of shifted echoes and $K$ are also provided in Figures S1 and S2. To summarize, the simulations suggest that shifting one-third of the echoes with a sufficiently large area of the additional gradients (e.g., $b \approx 200 \, \text{s/mm}^2$ for 64 echoes) optimizes the quantification results, with diffusion being quantified for CSF.

Figure 3 displays the results of the phantom experiments. The proposed ES-mGRE sequence produced echo images at very long TE values without significant artifacts. The signal intensity of the shifted echoes decreased as the $K$ values increased, in line with the theoretical prediction. The calculated $T_2^*$ and $D_z$ maps exhibited the same trends as the computer simulations. Without consideration of the diffusion effect, biased $T_2^*$ values were obtained. These values further deviated from the reference

**TABLE 2** Mean and standard deviation of the calculated $T_2^*$s and $D_z$ for each region of interest (ROI) using data acquired with 64 echoes and $K$ of 10 (21 shifted echoes with echo time starting from $\sim$210 ms).

| | ROI 1 | ROI 2 | ROI 3 | ROI 4 | ROI 5 |
|---|---|---|---|---|---|
| $T_2^*$ (ms) | $44.6 \pm 0.7$ | $63.1 \pm 1.4$ | $72.7 \pm 1.7$ | $90.0 \pm 1.6$ | $121.9 \pm 3.2$ |
| $D_z$ ($\mu m^2$/ms) | $0.5 \pm 0.4$ | $1.7 \pm 0.6$ | $2.2 \pm 0.6$ | $1.8 \pm 0.2$ | $2.0 \pm 0.2$ |
| Reference (In-house-implemented mGRE, QUTE) - $T_2^*$ | $44.5 \pm 0.4$ | $63.3 \pm 0.6$ | $72.8 \pm 1.1$ | $91.1 \pm 0.6$ | $122.6 \pm 2.7$ |
| Reference (DW-EPI) - $D_z$ | | | $2.1 \pm 0.02$ | | |

Abbreviations: DW-EPI, diffusion-weighted echo-planar imaging; mGRE, multi-echo gradient echo; QUTE, quantitative $T_2^*$ image.

when $K$ increased, especially in regions with relatively long $T_2^*$. The inclusion of the diffusion term in the fit allowed for $D_z$ and $T_2^*$ to be quantified, the latter with high accuracy. Increasing the area of the additional gradients improved the precision of $D_z$. Reducing the number of echoes required a larger area of additional gradients for similar precision. Table 2 lists the mean and standard deviation of $T_2^*$ and $D_z$ within each ROI, calculated from the data sets with 64 echoes and $K$ equal 10. The quantified values closely matched the reference values.

Figure 4 shows the results from in vivo experiments. In images produced by the standard reconstruction software of the scanner, artifacts from CSF at the ventricles were present across the entire brain region and became more pronounced in the long TE images. Overlap of the actual signal and artifacts alters the signal intensity, reducing the accuracy of the quantified metrics. However, these artifacts were eliminated with navigator echo correction, showing that navigators are imperative for accurate mapping of long $T_2^*$, or imaging at long TEs. Following visual inspection of the navigator-corrected $T_2^*$ maps, ES-mGRE offers clearer delineation of brain structures, such as the centrum semiovale, compared with the vendor-implemented Siemens GRE, which does not acquire navigation echoes. Conversely, the $T_2^*$ map from ES-mGRE data is similar to that of the reference method (i.e., QUTE with subechoes). The $T_2^*$ maps, with and without consideration of the diffusion term, are visually comparable. The last column in Figure 4C shows the map of corrected Akaike Information Criterion (cAIC) values, comparing the two fit methods.[36,37] Note that the cAIC values suggest that the incorporation of the diffusion term leads to a more accurate representation of the signal, particularly in CSF regions characterized by high diffusivity values. The method thus produces high-resolution, distortion-free diffusion maps of CSF.

Figure 5A illustrates the brain coverage of in-house-implemented mGRE and ES-mGRE. The ES-mGRE enables the acquisition of twice the number of slices compared with the mGRE within the same measurement time. Figure 5B presents comprehensive $T_2^*$

and $D_z$ maps of the whole brain obtained from ES-mGRE. Note that, in particular, it is possible to quantify the diffusivity values of CSF not only within the ventricles but also within the subarachnoid space with high resolution. Table 3 lists the statistical measures of the calculated $T_2^*$ and $D_z$ values compared with the reference methods. The mean $T_2^*$ values of gray and white matter agree with those obtained from the retrospectively subsampled mGRE. The median value for CSF $T_2^*$ was consistent with that from mGRE. In addition, the ES-mGRE-derived $D_z$ values were comparable to the values obtained by reference diffusion measurements. Across subjects, the average of the median $T_2^*$ values in the lateral ventricles was 276.5 ms, substantially higher than in the third (192.7 ms) and fourth ventricles (231 ms), and the subarachnoid space (114.3 ms). All pairwise comparisons between the lateral ventricles and other regions showed statically significant differences ($p < 0.0027$; Kolmogorov–Smirnov test). Similarly, the mean $D_z$ value in the subarachnoid space was lower than that in the lateral ventricle across all subjects, with all comparisons yielding $p$-values $< 7e-28$ (Kolmogorov–Smirnov test).

## 5 | DISCUSSION

In this study, an echo-shifting technique was combined with mGRE, an established method for high-quality $T_2^*$ mapping,[9–11] for the quantification of $T_2^*$ of CSF with high accuracy and precision. The use of additional gradients facilitated the acquisition of $T_2^*$-weighted images at long TEs without significantly increasing the scan time. The scan time is only prolonged by sub-TR (TR/no. of slices), which has a negligible duration of around 100 ms for the performed acquisition with 64 echoes. In our design, two additional gradients with an area ratio of $-1$:2 were periodically applied to shift the echoes. In principle, a single additional gradient could be used in an alternating manner (i.e., $-A$ for one sub-TR and A for the next sub-TR). Using fewer additional gradients might reduce the influence of eddy currents. However, the signals are
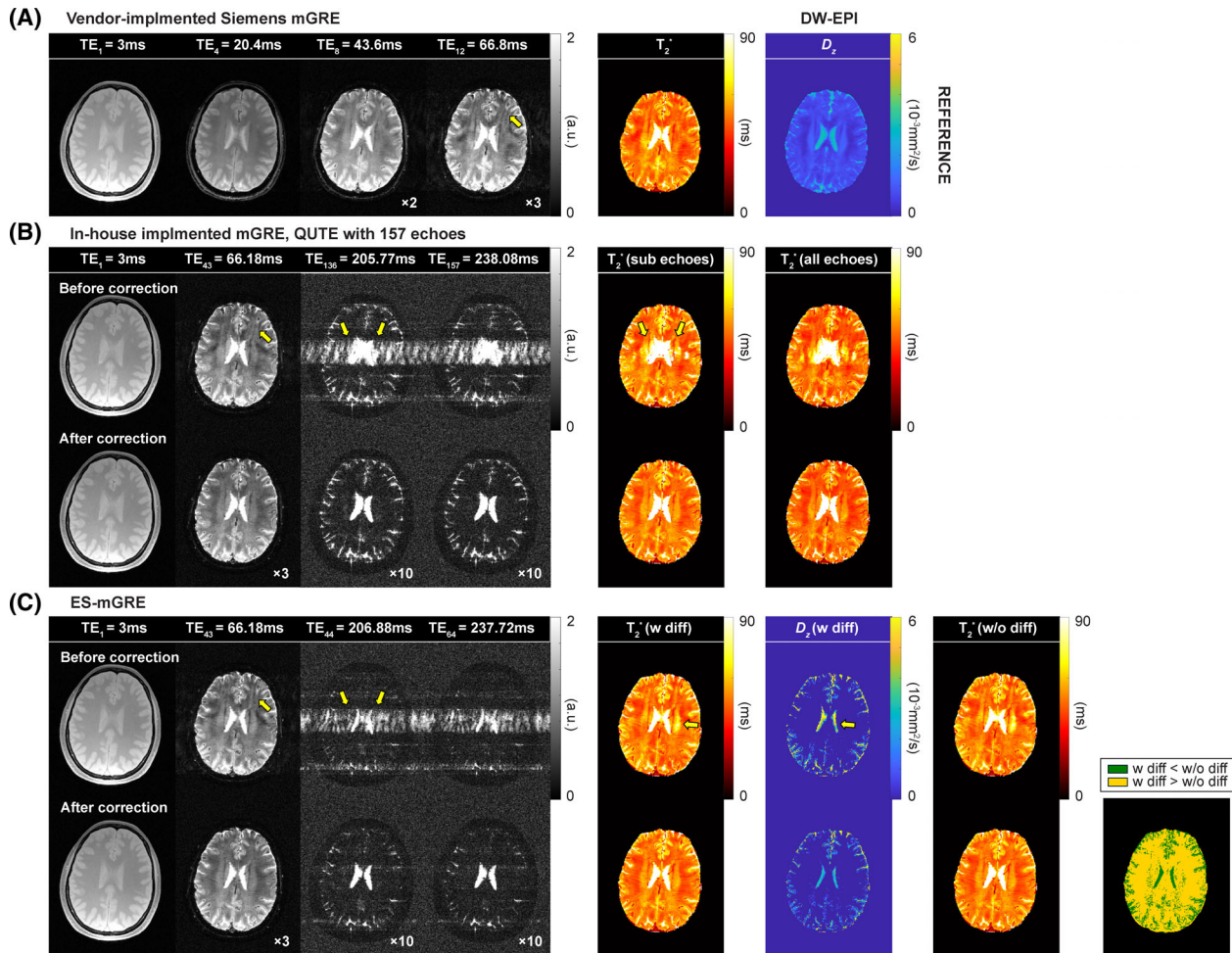
**FIGURE 4** Results of in vivo experiments obtained using vendor-implemented Siemens multi-echo gradient echo (mGRE) (A), in-house-implemented mGRE (B), quantitative $T_2^*$ image, and echo-shifted, multi-echo GRE (ES-mGRE) sequences (C). In (B) and (C), the first and second rows depict the results before and after applying the navigator echo correction, respectively. The first to fourth columns display the acquired images. The yellow arrows indicate the ghost artifacts induced by physiological fluctuations. The derived quantitative maps are presented next to the images. For the in-house-implemented mGRE data sets, the $T_2^*$ values were quantified after retrospectively selecting the images to match the echo time (TE) values of ES-mGRE (*fifth column*), as well as considering all acquired TE images (*sixth column*). In ES-mGRE, a map that compares corrected Akaike Information Criterion (cAIC) values is also displayed. The areas where the signal model with a diffusion term provides a better fit compared to the model without a diffusion term are indicated by the color green. Otherwise, it is represented by the yellow. DW-EPI, diffusion-weighted echo-planar imaging.

balanced in such a way that the spins excited from $n$th RF pulse would be rephased again after two sub-TR intervals and interfere with the signal from another slice. In the proposed sequence design, the signals from $n$th RF pulse are gradually dephased over time after acquiring shifted echoes (Figure 1B). ES-mGRE adopts an interleaved acquisition strategy, which circumvents the signal loss commonly associated with traditional echo-shifting techniques, where two pulses contribute to the signal from one slice.[22,23] The area of additional gradients needs to be considerable; otherwise, there is still a risk of signal contamination from previous slices. Optimization is required, as an excessive increase in the area of additional gradients can lead to a longer scan time, necessitating a reduction

in the number of echoes or slices obtainable within a given TR.

From the signal-fitting perspective, the lowest standard deviation of $T_2^*$ is achieved with a continuous and unshifted echo train. However, such an acquisition requires an increased scan time. Furthermore, covering an extensive range of TE does not necessarily provide additional information about the signal decay of tissue (Figure 1C). ES-mGRE addresses these limitations by selectively acquiring both short and long TE images within a shorter scan time, providing a practical balance between accuracy and efficiency.

Incorporating a diffusion term, $\exp(-b \cdot D)$, is crucial for the accurate quantification of $T_2^*$ with ES-mGRE,
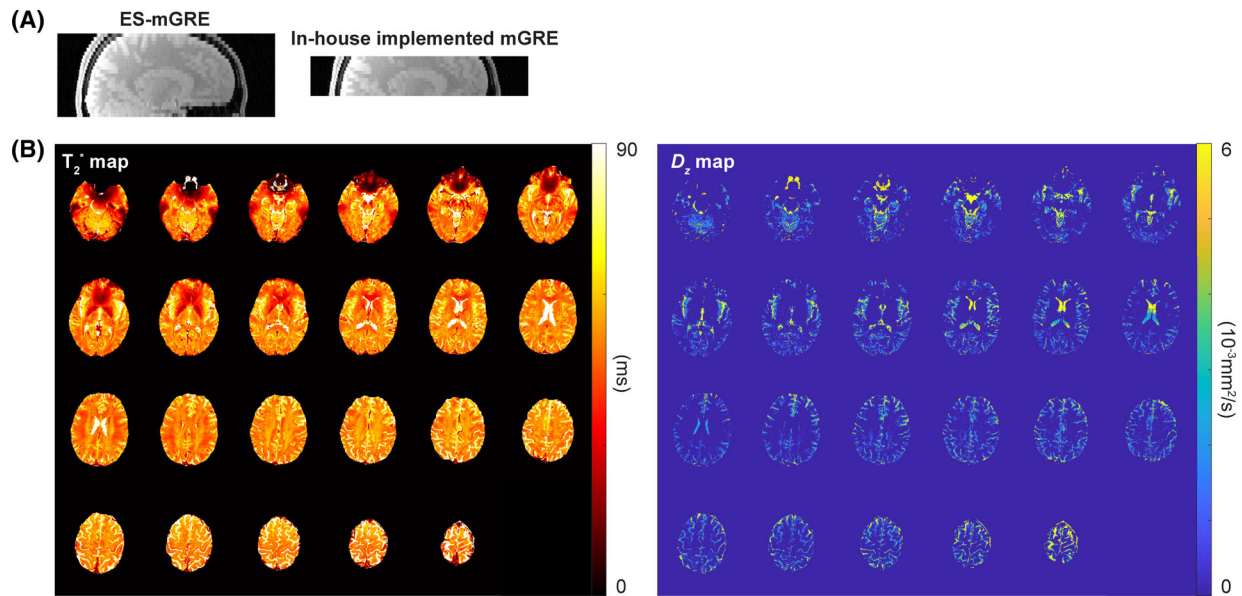
**FIGURE 5** (A) Brain coverage of in-house-implemented multi-echo gradient echo (mGRE) and echo-shifted mGRE (ES-mGRE). (B) Whole-brain $T_2$* and $D_z$ maps obtained from ES-mGRE.

**TABLE 3** Mean and standard deviation of the calculated $T_2$*s and $D_z$ from a single volunteer (*upper*) and across 4 subjects (*lower*).

| | GM | WM | Third ventricle | Fourth ventricle | Lateral ventricles | Subarachnoid space |
|---|---|---|---|---|---|---|
| $T_2$* (ms) | $54.6 \pm 11$ | $50.1 \pm 6.6$ | 216.7 (137.7, 479.9) | 276.4 (120.5, 521.3) | 304.2 (143.3, 786) | 119.9 (93.7, 186.1) |
| $T_2$* (without diffusion) | $54.5 \pm 11$ | $49.9 \pm 6.5$ | 105.4 (95.8, 112.5) | 106.7 (93.7, 110.8) | 133.8 (109.7, 181.4) | 102.4 (89.6, 124.0) |
| Reference (in-house-implemented mGRE, QUTE) - $T_2$* | $52.7 \pm 10.1$ | $47.8 \pm 6.4$ | - | - | 319.7 (165.6, 648.1) | 118.7 (94.4, 174.5) |
| Reference (in-house-implemented mGRE, QUTE with subechoes) - $T_2$* | $55.2 \pm 10.3$ | $49.9 \pm 6.3$ | - | - | 302.1 (159.7, 606.7) | 115.5 (93.5, 162.5) |
| $D_z$ (μm²/ms) | | | 3.13 (2.7, 4.5) | 3.32 (2.8, 4.3) | 3.3 (2.8, 4.1) | 3.01 (2.5, 3.8) |
| Reference (DW-EPI) - $D_z$ | | | 3.1 (2.4, 3.7) | 3.47 (3.14, 3.7) | 2.96 (2.69, 3.2) | 2.5 (2.23, 2.83) |
| Average values across subjects | | | | | | |
| $T_2$* | $55.9 \pm 1.8$ | $51.5 \pm 2.2$ | $192.7 \pm 29.4$ | $231 \pm 101.3$ | $276.5 \pm 42.3$ | $114.3 \pm 3.14$ |
| $D_z$ | | | $3.44 \pm 0.4$ | $3.54 \pm 0.3$ | $3.37 \pm 0.5$ | $3.02 \pm 0.4$ |

*Note*: The median, lower quartile (Q1), and upper quartile (Q3) were calculated for the cerebrospinal fluid regions ($80 \leq T_2$* $\leq 2000$ ms and $0.002 \leq D_z \leq 0.005$ mm²/s), given the fact that the distribution of values is not Gaussian. In the case of in-house-implemented multi-echo gradient echo, the information from the third and fourth ventricles was not obtained due to its limited slice coverage.

Abbreviations: DW-EPI, diffusion-weighted echo-planar imaging; GM, gray matter; mGRE, multi-echo gradient echo; QUTE, quantitative $T_2$* image; WM, white matter.

as the signal loss between unshifted and shifted echoes is influenced by the diffusion-weighting effect of the echo-shifting gradients. However, depending on the tissue properties and sequence parameters, the inclusion of the diffusion term may introduce instability in the fit and reduce the precision of the quantification, as shown by the simulation results (Figure S2). The slightly increased standard deviation of $T_2$* for ES-mGRE compared with in-house-implemented mGRE primarily arises due to this added complexity in the fit. Nevertheless, despite this minor trade-off, it enables simultaneous mapping of $T_2$* and diffusivity of CSF with high accuracy.

In principle, increasing the area of the additional gradients magnifies the difference in the intensity of the

unshifted versus the shifted echo signals, which aids in determining $T_2^*$ and diffusivity values. However, for tissues with short $T_2^*$ and/or large diffusivity values, excessively large gradients may overly suppress the intensity of the shifted echoes. Thus, setting appropriate imaging parameters is crucial for accurate and precise quantification and will depend on the characteristics of the tissue properties to be quantified. The use of 64 echoes (21 shifted) produced accurate and precise $T_2^*$ mapping for brain tissue and demonstrated good accuracy and precision in the $T_2^*$ and $D$ mapping for CSF, as shown both by simulations and experimental comparison with standard measurements.

The use of computer simulations allowed for the optimization of imaging parameters and the selection of the signal model. Although opting for a mono-exponential fitting without the diffusion term might compromise the accuracy of the quantification of $T_2^*$, this approach enhances its precision, as the number of free variables is reduced. When the additional gradients have a small area, and the number of shifted echoes is less than one-third of the total echoes, the discrepancy in the quantified $T_2^*$ values—with or without the inclusion of a diffusion term—is negligible, particularly in low diffusivity regions, such as brain tissue. Conversely, when using larger additional gradients, fitting without the diffusion term yields a marked deviation from the true $T_2^*$ values. This deviation can be quantified from simulations for given values or ranges of $T_2^*$ and diffusivity, as shown in this work. Thus, even without explicitly modeling the diffusion term, ES-mGRE represents a valuable tool for intersubject or intrasubject comparison with high sensitivity. Alternatively, $T_2^*$ can also be calculated using the $D$ values predefined from other literature or sequences, thereby reducing the number of variables in a fit.

With the optimized settings used in this work, ES-mGRE was able to obtain twice the number of slices compared with the in-house-implemented mGRE sequence within the same scan time. Alternatively, mGRE requires doubled acquisition time to achieve the same number of slices. Therefore, in the time required for mGRE, several ES-mGRE data sets can be obtained, such as with two optimized acquisition parameters to allow for adequate quantification in both tissue and CSF. Alternatively, because the $b$-value range from the echo-shifting gradients is relatively low ($< 300\,\text{s/mm}^2$), one could use several $b$-values to investigate tissue perfusion using the intravoxel incoherent motion technique.[38,39]

Notably, according to the spoiled GRE equation (Eq. [1]), the signal intensity increases nonlinearly with TR, and the additional signal gain resulting from increasing TR becomes marginal at longer TRs. For instance, doubling TR from 3000 ms to 6000 ms (assuming a $T_1$ of 4300 ms for CSF and adjusting the corresponding Ernst angle) results in only a 34% increase in signal. The trade-off, evaluated as SNR/acquisition time, is inefficient, given that doubling the scan time leads to less than twice SNR. This theoretical consideration emphasizes ES-mGRE as a more practical and time-efficient strategy for achieving greater spatial coverage without increasing TR.

Navigator echoes were acquired to correct for artifacts induced by physiological motion. Using navigator echoes from a relatively short TE allows for the precise estimation of resonance frequency ($f0$) variations. However, the $f0$ variation calculated from short TE navigators might not represent those present at longer TEs. Thus, the acquisition protocol was configured to obtain several navigator echoes along the echo train, separately for the unshifted and shifted echoes. However, using navigator echoes obtained at long TE poses a challenge due to the low SNR in brain parenchyma, which complicates the calculation of phase differences. Too low SNR at a specific position, $x$, causes spikes in the calculated phase difference and enhances instead of reducing artifacts in the images. For voxels with SNR values below average, the median value of the higher SNR regions was used to correct the global field variations.

The calculated $D_z$ values in the phantom experiments matched the reference values in regions with relatively large $T_2^*$ values when $K$ was large. However, in regions with shorter $T_2^*$ values, obtaining accurate values of $D_z$ was unsuccessful, even at larger $K$ values. This is because during the acquisition of the shifted echoes, the signals characterized by shorter $T_2^*$ are already decayed. To accurately quantify the $D_z$ values for the short $T_2^*$ regions, an effective approach can be to reduce the number of echoes, thereby decreasing the sub-TR and TEs of shifted echoes (Figure 3B). With a reduced number of echoes, ES-mGRE can still provide reliable $T_2^*$ quantification owing to its capability to acquire shifted echo images in the next sub-TR interval and thus extend the $T_2^*$ fitting range to an adequate TE interval. This applies to both phantom and in vivo data. Although diffusivity quantification in brain tissue and/or CSF remains a secondary benefit (Figure 6), the key advantage of this work lies in the robust and efficient $T_2^*$ mapping that ES-mGRE offers.

The quantified $D_z$ of CSF in vivo depends on the location within the ventricles. The values were consistent and comparable to those reported in the literature for the central part of the ventricles but were found to be larger toward the anterior horn/lower part of the ventricles. A possible cause is that these areas exhibit a faster $T_2^*$ decay, leading to less signal in the shifted echo images. A possible explanation of this observation is that the ventricles are composed of complex structures, including the highly irrigated choroid plexus and further blood vessels,[40] and it is
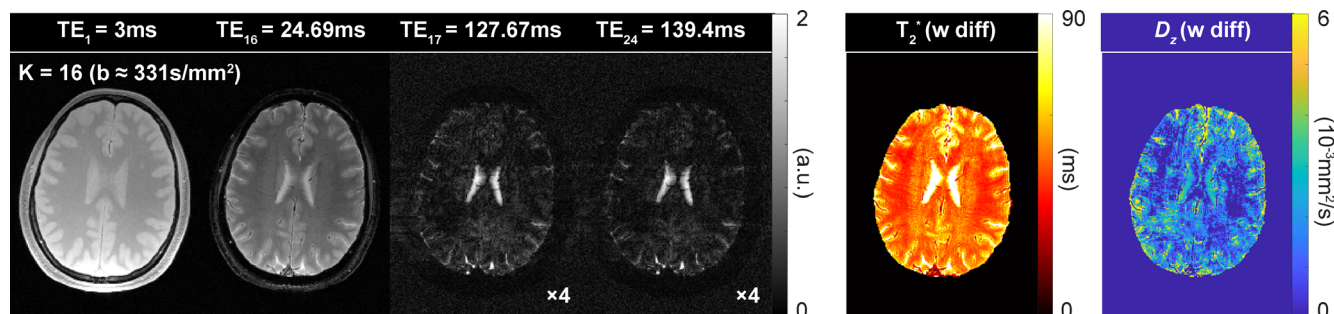
**FIGURE 6** Acquired images and calculated quantitative maps when using the data sets with 24 echoes. TE, echo time.

possible that susceptibility effects might contribute to the obtained values. Locally varying oxygenation of CSF could also affect $T_2^*$. A more likely cause for the increased $D_z$ and decreased $T_2^*$ is the presence of flow, but this is not currently included in the simulations or fit model. Recent studies have shown that $D^*$ from the intravoxel incoherent motion technique can reflect CSF flow.[41,42] In our work, $D_z$ was calculated with relatively small $b$-values. A simple diffusion term in our model, $D_z$, while limited, can still partially provide information on CSF dynamics.

For most brain tissues with intermediate $T_2^*$ and relatively low diffusivity, the diffusion coefficient is, at best, an estimate. However, if diffusivity and $T_2^*$ are increased in brain tissue, for example, in the case of pathologies such as vasogenic edema [38] or white-matter hyperintensities,[43] ES-mGRE *may offer the additional benefit* of simultaneous high-resolution diffusion estimate, in addition to accurate $T_2^*$ mapping in the affected regions. A natural application of our sequence is the investigation of long-$T_2^*$ free water in brain parenchyma, known to be associated with aging and/or neurodegeneration.[40,44–46] This can be done either by quantifying the intensity of very long echo images, or (better) by multicomponent evaluation of the signal.

It should be noted that $D_z$ is not a rotationally invariant metric. In this regard, a more complete characterization of water diffusion could be obtained by combining measurements with different orientations of the echo-shifting gradients. Although this would substantially increase the measurement time, the possibility of obtaining diffusion maps with perfect anatomical fidelity and high resolution is promising. A further possibility would be to adapt single-shot trace diffusion-weighting schemes[47,48] to our purposes. However, this is beyond the scope of the present work.

The present implementation of ES-mGRE was designed to shift part of the echoes into the next sub-TR interval. It is also feasible to acquire additional shifted echoes after two or more sub-TR intervals with an appropriate sequence design. However, a limitation of an increasing number of echo intervals is that the TEs of shifted echoes are constrained by the total number of echoes and sub-TR values, and thus, numerical optimization considering the $T_2^*$ of targeted regions is required.

## 6 | CONCLUSIONS

A novel ES-mGRE sequence has been proposed in this study. By using additional gradients, both short and long TE images can be acquired without a substantial increase in acquisition time. The use of navigator echoes to correct for phase variations both between k-space lines and along the echo train was found to be crucial for image and quantification quality. The obtained images allowed for simultaneous quantification of $T_2^*$ and 1D diffusivity/flow in CSF.

### ORCID
*Seonyeong Shin* https://orcid.org/0000-0002-1742-8105
*Ana-Maria Oros-Peusquens* https://orcid.org/0000-0003-1869-3354
*Seong Dae Yun* https://orcid.org/0000-0001-7398-1899
*N. Jon Shah* https://orcid.org/0000-0002-8151-6169

### REFERENCES
1. Otsuji R, Fujioka Y, Hata N, et al. Liquid biopsy for glioma using cell-free DNA in cerebrospinal fluid. *Cancer*. 2024;16:1009. doi:10.3390/cancers16051009

2. Jessen NA, Munk AS, Lundgaard I, Nedergaard M. The glymphatic system: a beginner's guide. *Neurochem Res*. 2015;40:2583-2599. doi:10.1007/s11064-015-1581-6

3. Hablitz LM, Nedergaard M. The glymphatic system: a novel component of fundamental neurobiology. *J Neurosci*. 2021;41:7698-7711. doi:10.1523/JNEUROSCI.0619-21.2021

4. Klostranec JM, Vucevic D, Bhatia KD, et al. Current concepts in intracranial interstitial fluid transport and the glymphatic system. Part I: Anatomy and physiology. *Radiology*. 2021;301:502-514. doi:10.1148/radiol.2021202043

5. Spijkerman JM, Petersen ET, Hendrikse J, Luijten P, Zwanenburg JJM. T2 mapping of cerebrospinal fluid: 3 T versus 7 T. *MAGMA*. 2018;31:415-424. doi:10.1007/s10334-017-0659-3

6. Xue Y, Liu X, Koundal S, et al. In vivo T1 mapping for quantifying glymphatic system transport and cervical lymph node drainage. *Sci Rep*. 2020;10:14592. doi:10.1038/s41598-020-71582-x

7. Watts R, Steinklein JM, Waldman L, Zhou X, Filippi CG. Measuring glymphatic flow in man using quantitative contrast-enhanced MRI. *AJNR Am J Neuroradiol*. 2019;40:648-651. doi:10.3174/ajnr.A5931

8. Harrison IF, Siow B, Akilo AB, et al. Non-invasive imaging of CSF-mediated brain clearance pathways via assessment of perivascular fluid movement with diffusion tensor MRI. *Elife*. 2018;7:e34028. doi:10.7554/eLife.34028

9. Shah NJ, Zaitsev M, Steinhoff S, Wiese S, Zilles K. Development of sequences for fMRI: keyhole imaging and relaxation time mapping. In: *Proceedings of the 15th European Experimental NMR Conference* 2000.

10. Dierkes T, Neeb H, Shah NJ. Distortion correction in echo-planar imaging and quantitative T2* mapping. *Int Congr Ser*. 2004;1265:181-185.

11. Shin S, Yun SD, Shah NJ. $T_2$* quantification using multi-echo gradient echo sequences: a comparative study of different readout gradients. *Sci Rep*. 2023;13:1138. doi:10.1038/s41598-023-28265-0

12. Neeb H, Dierkes T, Shah NJ. Quantitative $T_1$ mapping and absolute water content measurement using MRI. *Int Congr Ser*. 2004;1265:113-123.

13. Neeb H, Ermer V, Stocker T, Shah NJ. Fast quantitative mapping of absolute water content with full brain coverage. *Neuroimage*. 2008;42:1094-1109.

14. Shah NJ, Neeb H, Kircheis G, Engels P, Häussinger D, Zilles K. Quantitative cerebral water content mapping in hepatic encephalopathy. *Neuroimage*. 2008;41:706-717. doi:10.1016/j.neuroimage.2008.02.057

15. Shah NJ, Ermer V, Oros-Peusquens AM. Measuring the absolute water content of the brain using quantitative MRI. In: Modo M, Bulte J, eds. *Magnetic Resonance Neuroimaging. Methods in Molecular Biology*. Vol 711. Humana Press; 2011. doi:10.1007/978-1-61737-992-5_3

16. Shin S, Yun S, Shah NJ. Fast and whole-brain $T_2$* mapping using QUTE-EPI at 7T. *In: Proceedings of the 27th Annual Meeting of ISMRM, Montreal, Canada*. 2019:4418.

17. Shin S, Oros-Peusquens A, Yun S, Farrher E, Shah NJ. Development of a novel sequence for $T_2$* quantification of slow-relaxing water pools in the brain. *In: Proceedings of the 31st Annual Meeting of ISMRM, Toronto, Canada*. 2023;0666

18. Griswold MA, Kannengiesser S, Heidemann RM, Wang J, Jakob PM. Field-of-view limitations in parallel imaging. *Magn Reson Med*. 2004;52:1118-1126. doi:10.1002/mrm.20249

19. Deshmane A, Gulani V, Griswold MA, Seiberlich N. Parallel MR imaging. *J Magn Reson Imaging*. 2012;36:55-72. doi:10.1002/jmri.23639

20. Moonen CT, Liu G, van Gelderen P, Sobering G. A fast gradient-recalled MRI technique with increased sensitivity to dynamic susceptibility effects. *Magn Reson Med*. 1992;26:184-189. doi:10.1002/mrm.1910260118

21. Denolin V, Metens T. On the calculation and interpretation of signal intensity in echo-shifted sequences. *Magn Reson Med*. 2003;51:123-134. doi:10.1002/mrm.10657

22. Ma YJ, Liu W, Zhao X, et al. 3D interslab echo-shifted FLASH sequence for susceptibility weighted imaging. *Magn Reson Med*. 2016;76:222-228. doi:10.1002/mrm.25872

23. Ehses P, Bause J, Shajan G, Scheffler K. Efficient generation of $T_2$*-weighted contrast by interslice echo-shifting for human functional and anatomical imaging at 9.4 Tesla. *Magn Reson Med*. 2015;74:1698-1704. doi:10.1002/mrm.25570

24. Versluis MJ, Peeters JM, van Rooden S, et al. Origin and reduction of motion and f0 artifacts in high resolution $T_2$*-weighted magnetic resonance imaging: application in Alzheimer's disease patients. *Neuroimage*. 2010;51:1082-1088. doi:10.1016/j.neuroimage.2010.03.048

25. Wen J, Cross AH, Yablonskiy DA. On the role of physiological fluctuations in quantitative gradient echo MRI: implications for GEPCI, QSM, and SWI. *Magn Reson Med*. 2015;73:195-203. doi:10.1002/mrm.25114

26. Walsh DO, Gmitro AF, Marcellin MW. Adaptive reconstruction of phased array MR imagery. *Magn Reson Med*. 2000;43:682-690. doi:10.1002/(sici)1522-2594(200005)43:5<682::aid-mrm10>3.0.co;2-g

27. Güllmar D, Haueisen J, Reichenbach JR. Analysis of b-value calculations in diffusion weighted and diffusion tensor imaging. *Concepts Magn Reson*. 2025;25A:53-66. doi:10.1002/cmr.a.20031

28. Delakis I, Petala K, De Wilde JP. MRI receiver frequency response as a contributor to Nyquist ghosting in echo planar imaging. *J Magn Reson Imaging*. 2005;22:324-328. doi:10.1002/jmri.20365

29. Yu H, McKenzie CA, Shimakawa A, et al. Multiecho reconstruction for simultaneous water-fat decomposition and $T_2$* estimation. *J Magn Reson Imaging*. 2007;26:1153-1161. doi:10.1002/jmri.21090

30. Peterson P, Månsson S. Fat quantification using multiecho sequences with bipolar gradients: investigation of accuracy and noise performance. *Magn Reson Med*. 2014;71:219-229. doi:10.1002/mrm.24657

31. Sandino CM, Kellman P, Arai AE, Hansen MS, Xue H. Myocardial $T_2$* mapping: influence of noise on accuracy and precision. *J Cardiovasc Magn Reson*. 2015;17:7.

32. Raya JG, Dietrich O, Horng A, Weber J, Reiser MF, Glaser C. $T_2$ measurement in articular cartilage: impact of the fitting method on accuracy and precision at low SNR. *Magn Reson Med*. 2010;63:181-193. doi:10.1002/mrm.22178

33. Sijbers J, den Dekker AJ, Raman E, Van Dyck D. Parameter estimation from magnitude MR images. *Int J Imaging Syst Technol*. 1999;10:109-114.

34. Dale AM, Fischl B, Sereno MI. Cortical surface-based analysis. I. Segmentation and surface reconstruction. *Neuroimage*. 1999;9:179-194. doi:10.1006/nimg.1998.0395

35. Fischl B, Salat DH, Busa E, et al. Whole brain segmentation: automated labeling of neuroanatomical structures in the human brain. *Neuron*. 2002;33:341-355. doi:10.1016/s0896-6273(02)00569-x

36. Burnham KP, Anderson DR. Information theory and log-likelihood models: a basis for model selection and inference. *Model Selection and Inference*. Springer; 1998:49-97. doi:10.1007/978-1-4757-2917-7_2

37. Farrher E, Chiang CW, Cho KH, et al. Spatiotemporal characterisation of ischaemic lesions in transient stroke animal models using diffusion free water elimination and mapping MRI with echo time dependence. *Neuroimage*. 2021;244:118605. doi:10.1016/j.neuroimage.2021.118605

38. Loução R, Oros-Peusquens AM, Langen KJ, et al. A fast protocol for multiparametric characterisation of diffusion in the brain and brain tumours. *Front Oncol*. 2021;11:554205. doi:10.3389/fonc.2021.554205

39. Le Bihan D. What can we see with IVIM MRI? *Neuroimage*. 2019;187:56-67. doi:10.1016/j.neuroimage.2017.12.062

40. Stratchko L, Filatova I, Agarwal A, Kanekar S. The ventricular system of the brain: anatomy and normal variations. *Semin Ultrasound CT MR*. 2016;37:72-83. doi:10.1053/j.sult.2016.01.004

41. Voorter PHM, Jansen JFA, van der Thiel MM, et al. Diffusion-derived intravoxel-incoherent motion anisotropy relates to CSF and blood flow. *Magn Reson Med*. 2025;93:930-941. doi:10.1002/mrm.30294

42. Jang M, Han S, Cho H. D* from diffusion MRI reveals a correspondence between ventricular cerebrospinal fluid volume and flow in the ischemic rodent model. *J Cereb Blood Flow Metab*. 2021;42:572-583. doi:10.1177/0271678X211060741

43. Iordanishvili E, Schall M, Loução R, et al. Quantitative MRI of cerebral white matter hyperintensities: a new approach towards understanding the underlying pathology. *Neuroimage*. 2019;202:116077. doi:10.1016/j.neuroimage.2019.116077

44. Gong T, Tong Q, He H, Sun Y, Zhong J, Zhang H. MTE-NODDI: multi-TE NODDI for disentangling non-$T_2$-weighted signal fractions from compartment-specific $T_2$ relaxation times. *Neuroimage*. 2020;217:116906. doi:10.1016/j.neuroimage.2020.116906

45. Planetta PJ, Ofori E, Pasternak O, et al. Free-water imaging in Parkinson's disease and atypical parkinsonism. *Brain*. 2016;139:495-508. doi:10.1093/brain/awv361

46. Canales-Rodríguez EJ, Alonso-Lana S, Verdolini N, et al. Age- and gender-related differences in brain tissue microstructure revealed by multi-component T2 relaxometry. *Neurobiol Aging*. 2021;106:68-79. doi:10.1016/j.neurobiolaging.2021.06.002

47. Mori S, van Zijl PC. Diffusion weighting by the trace of the diffusion tensor within a single scan. *Magn Reson Med*. 1995;33:41-52. doi:10.1002/mrm.1910330107

48. Chun T, Uluğ AM, van Zijl PC. Single-shot diffusion-weighted trace imaging on a clinical scanner. *Magn Reson Med*. 1998;40:622-628. doi:10.1002/mrm.1910400415

## SUPPORTING INFORMATION

Additional supporting information may be found in the online version of the article at the publisher's website.

**Figure S1.** Reference (A) and calculated (B–D) $T_2^*$ and $D$ maps with respect to the number of echoes and areas of additional gradients. (B,C,D) Results from data sets with 24, 32, and 64 echoes, respectively, where one-third of the echoes were shifted. The $K$ and corresponding $b$-values of the shifted echoes are written in each row.

**Figure S2.** Plots of the mean and standard deviation of the calculated $T_2^*$s and $D$s in each region of interest (ROI). (A–C) Data sets with 24, 32, and 64 echoes, respectively. In each panel, the first and second rows show the mean and standard deviation of the diffusion-considered $T_2^*$s, whereas the third and fourth rows show the mean and standard deviation of the calculated $D$s. The mean and standard deviations of the $T_2^*$s when the diffusion effect was not considered are shown in the fifth and sixth rows. The x-axis is the number of shifted echoes. Each color denotes the different area of the additional gradients.

**Figure S3.** Results of phantom experiments with respect to the number of echoes. (A–C) Images and quantitative parameter maps acquired from the data sets having 24, 32, and 64 echoes, respectively. In each panel, the fifth and sixth columns present the $T_2^*$ and $D$ maps, whereas the seventh column shows the $T_2^*$ maps calculated without considering the diffusion term in a fit model.

**Table S1.** Imaging parameters for phantom experiments when the number of echoes was 24 (A), 32 (B), and 64 (C). The number of slices was set to be the maximum possible, while minimizing the time required for additional gradients.

**Table S2.** Imaging parameters for diffusion-weighted echo-planar imaging (DW-EPI) and three-dimensional magnetization-prepared rapid gradient-echo (MP-RAGE) sequences used in in vivo experiments.